International Journal of Electrochemical Science 20 (2025) 101027

Contents lists available at ScienceDirect

International Journal of Electrochemical Science

journal homepage: www.editorialmanager.com/ijoes

# Comparative analysis of electrochemical properties and thermal behaviors of sodium ion and lithium ion batteries

Han Xu [a], Guoqing Zhang [a], Jiantao Zhang [a], Jiangyun Zhang [a,*], Hongwei Wu [b], Liqin Jiang [c], Wenzhao Jiang [c], Jun Liu [d], Kang Peng [d]

[a] *School of Materials and Energy, Guangdong University of Technology, Guangzhou 510006, China*
[b] *School of Physics, Engineering and Computer Science, University of Hertfordshire, Hatfield AL10 9AB, United Kingdom*
[c] *Guangdong Zhuhai Supervision Testing Institute of Quality and Metrology, Zhuhai 519000, China*
[d] *Guangdong Greenway Technology Co., Ltd, Dongguan 523000, China*

ARTICLE INFO

*Keywords:*
Sodium-ion batteries
Lithium-ion batteries
Electrochemical performance
Heat production characteristics
Thermal runaway

ABSTRACT

Sodium-ion batteries (SIBs), characterized by their abundant raw material sources and cost-effective manufacturing processes, have emerged as one of the most promising battery technologies. However, the existing literature on the electrochemical and thermal generation characteristics of SIBs remains limited. This dissertation conducts a comparative investigation of the electrical-thermal properties of 18650-type SIBs and Lithium-ion batteries (LIBs) from both macroscopic and microscopic perspectives. The initial phase of the study involved conducting experiments under standard operating conditions, with variations in ambient temperatures and discharge rates. Furthermore, investigations into overcharging and thermal runaway (TR) were conducted under extreme conditions, with concurrent studies on heat generation and electrochemical analyses. The underlying mechanisms responsible for macroscopic performance variations were elucidated through microstructural characterization.

The experimental findings reveal that at an ambient temperature of 0 °C, the State of Charge (SOC) of Sodium-Ion Batteries (SIBs) exceeds that of Lithium-Ion Batteries (LIBs) by 13.93 %. Under standard operating conditions, LIBs demonstrate enhanced cyclic capacity retention relative to SIBs, albeit with higher thermal generation. Under abusive conditions, the performance of SIBs markedly deteriorates, accompanied by a substantial increase in heat generation, surpassing that of LIBs. Following abuse, SIBs experience thermal runaway, attaining a peak temperature of 273.9 °C. The performance degradation is primarily attributed to severe sodium deposition on the anode and the subsequent detachment of active materials. These findings furnish essential experimental data and theoretical underpinnings for the industrial deployment of SIBs, while providing critical insights for optimizing their production processes and improving thermal safety performance.

## 1. Introduction

Lithium-ion batteries (LIBs) have become the industry standard due to their superior performance, which includes high energy density, extended cycle life, no memory effect, and low environmental pollution [1–6]. Under conditions of mechanical, thermal, or electrical abuse [7–15], the battery produces excessive heat within a confined space, resulting in thermal runaway (TR) and potentially severe thermal disasters.

Extensive research has been conducted on the thermal safety issues of LIBs. Among the various strategies for thermal safety management, an effective approach involves the incorporation of external functional materials to mitigate or delay the thermal runaway process. These materials significantly enhance the thermal stability of battery systems through mechanisms such as physical barrier formation, heat absorption, or chemical reactions [16–19]. Another area of research focuses on conducting thermal runaway tests under varying parameters or operational conditions, encompassing the influence of fundamental electrochemical parameters on thermal safety. Hu et al. [20] investigated the thermally induced TR process at varying current rates, demonstrating that the cell exhibited higher TR onset and peak temperatures as the current rates increased. Wang et al. [21] employed varying charging rates to induce TR in LIB through overcharging. The study revealed that

---

* Corresponding author.
*E-mail address:* roseyyun@163.com (J. Zhang).

https://doi.org/10.1016/j.ijoes.2025.101027
Received 3 March 2025; Received in revised form 26 March 2025; Accepted 10 April 2025

**Nomenclature**

| | |
|---|---|
| SIBs | Sodium-ion batteries |
| LIBs | Lithium-ion batteries |
| SOC | State of charge |
| TR | Thermal runaway |
| NB | Normal battery |
| OB | Overcharged battery |
| ARC | Acceleration rate calorimeter |
| SEM | Scanning electron microscopy |
| $R_{oh}$ | ohmic resistance |
| $R_{ct}$ | Charge transfer resistance |
| CC | Constant current |
| CV | Constant voltage |
| V | Voltage |
| $T_{max}$ | Maximum temperature |
| EIS | Electrochemical impedance spectroscopy |
| DMC | Dimethyl carbonate |

as the charging rate increases, the growth rate of lithium dendrites accelerates, resulting in the earlier formation of large-scale short circuits and a rapid transition to the next stage of the TR chain reaction. Xu et al. [22] investigated the influence of diverse operating conditions on the internal parameters and TR characteristics of the battery, demonstrating that an elevated charging rate is associated with a higher peak TR temperature. Liu et al. [23] analyzed the thermal stability of LIBs under conditions of minor overcharging, demonstrating that the increase in heat generation following overcharging is primarily due to a rise in the battery's internal. Kong et al. [24] investigated the impact of operating temperature on the TR and combustion characteristics of LIBs. The experimental results demonstrated that a decrease in operating temperature from 25 °C to −10 °C significantly reduces the TR onset temperature of LIBs. Low-temperature cycling induces cracking of the safety valves, leading to premature initiation of TR. Ohneseit et al. [25] analyzed the safety and TR characteristics of three LIBs employing NCM, NCA, and LFP as cathode material. NCM batteries exhibited the earliest initiation of exothermic reactions, while NCA batteries transitioned to thermal runaway at a faster rate compared to NCM batteries. Huang et al. [26] conducted a comparative analysis of the TR propagation characteristics between NCM and LFP modules. The results indicated that NCM modules displayed intense ejection ignition and combustion behavior, while LFP modules generated only a significant volume of white smoke. Mao et al. [27] employed an acceleration rate calorimeter (ARC) to investigate the self-heating reactions of LIBs at various SOCs. They discovered that fully charged LIBs are capable of self-ignition when maintained at temperatures exceeding 149.6 °C under natural convection conditions. Liu et al. [28] investigated the impact of batteries with different SOCs on fire behavior in a confined enclosure. The results demonstrated that an increase in the batteries' SOC within the confined enclosure led to enhanced heat release and more severe TR events. An et al. [29] analyzed cylindrical lithium-ion batteries (LIBs) with varying SOCs during three-point bending tests. They observed that a higher SOC is associated with an increased average heating rate of the battery. When the SOC exceeds 60 %, the battery is prone to severe TR events, such as explosion and fire emission, subsequent to the bending test. Research on the thermal safety of LIBs is extensive, encompassing performance evaluations across multiple dimensions, such as varying charge and discharge rates, operating temperatures, battery chemistries, SOCs, and temperature rise rates [30]. The thermal safety assessment of SIBs, an emerging and highly promising battery technology, is of critical importance.

Sodium-ion batteries (SIBs) offer numerous advantages, such as abundant raw material availability, straightforward extraction processes, and cost-effectiveness. These attributes have driven extensive research in energy storage and low-speed electric vehicles [31–35], garnering significant attention from both industrial and academic sectors. SIBs operate similarly to LIBs, as both store and release energy through the movement of ions between the anode and cathode [36,37].

In comparison to LIBs, research on the thermal safety of SIBs remains relatively limited. Significant attention and enhanced research efforts are required to comprehensively address the thermal safety challenges associated with SIBs.

Yue et al. [38] conducted a comprehensive investigation into the TR characteristics and associated hazards of SIBs utilizing NTM ($Na_xTMO_2$) as the cathode material, compared to LIBs employing LFP and NCM as cathode materials, respectively. Their findings revealed that the TR hazards of NTM-based SIBs fall between those of LFP and NCM-based LIBs, with a higher propensity to manifest compared to LFP-based systems. Xie et al. [39] systematically investigated the thermal runaway behavior of a 1000 mA h soft-pack sodium-ion battery with a $NaNi_{1/3}Fe_{1/3}Mn_{1/3}O_2$/hard carbon configuration. Their analysis demonstrated that the onset temperature for thermal runaway ($T_1$) occurred at 166.3 °C, coinciding with the initiation of cell bloating. Subsequently, the battery temperature rose to a characteristic temperature ($T_2$) of 243.4 °C, followed by a rapid and abrupt surge, reaching a peak temperature ($T_3$) of 312.24 °C within seconds. According to Zhou et al. [40], TR study was conducted on high-power 26,650 cylindrical SIBs, revealing that the SIBs exhibited greater thermal stability than LIBs, with initial decomposition temperatures exceeding 110 °C and maximum thermal runaway temperatures below 350 °C. A. Bordes et al. [41] investigated the gas production characteristics of 18650 cylindrical SIBs ($Na_3V_2(PO_4)_2F_3$) under thermal abuse conditions. The gas composition produced during thermal runaway in sodium-ion batteries is similar to that of LIBs.

The aforementioned literature primarily focuses on separate investigations into the thermal safety issues of lithium-ion batteries (LIBs) and sodium-ion batteries (SIBs). However, there is a notable lack of research on the thermal safety of SIBs under various conditions, such as different rates, ambient temperatures, and overcharge abuse scenarios. To address these gaps, this study systematically compares the fundamental thermoelectrochemical characteristics of 18650-type SIBs and LIBs under both normal operating conditions and abuse conditions. Initially, under normal operating conditions, the effects of ambient temperature and discharge rates on the capacity and exothermic behavior of both LIBs and SIBs were systematically investigated. Subsequently, under overcharge abuse conditions, the electro-thermal characteristics of the two battery types, including their TR behaviors, were analyzed across varying degrees of overcharge. Based on the macroscopic findings, the batteries were disassembled for microstructural analysis, which elucidated the fundamental mechanisms underlying the observed electro-thermal performance variations. This research provides a scientific foundation and valuable empirical data for optimizing battery manufacturing technologies. Furthermore, it offers systematic theoretical guidance and experimental support for enhancing the thermal-electrochemical performance and thermal safety of both sodium-ion and lithium-ion batteries.

## 2. Experimental design

### 2.1. Selection of test batteries

This study employed 18650-type SIBs (procured from Jiangsu Transimage Sodium-ion Battery Technology Co., Ltd.) and LIBs (procured from Guangzhou Jieli New Energy Co., Ltd.) with closely matched nominal capacities as experimental subjects. The physical appearance and technical specifications of the two battery types are illustrated in Fig. 1 and Table 1, respectively. The procedure for assessing the initial capacity consistency of the cells was as follows: three cells were randomly selected for each type and labeled according to their category

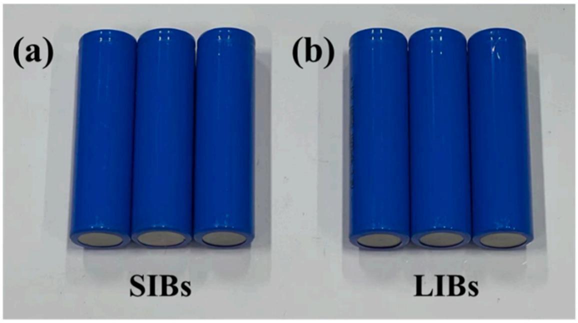

**Fig. 1.** Test the physical condition of the battery: (a) SIBs; (b) LIBs.

**Table 1**
Battery technical specifications for SIBs and LIBs.

| Items | SIB | LIB |
|---|---|---|
| Cathode and anode materials | $Na(Ni_{0.4}Fe_{0.2}Mn_{0.4})O_2$/HC | LiFePO4/C |
| Nominal voltage, V | 3.1 | 3.2 |
| Nominal capacity, mAh | 1300 | 1500 |
| Charging cut-off voltage, V | 3.95 | 3.65 |
| Maximum charging current, A | 1.3 | 1.5 |
| Maximum discharge current, A | 3.9 | 4.5 |
| Discharge cut-off voltage, V | 1.5 | 2.0 |
| Operating temperature interval, °C | Charging: −10–45<br>Discharging: −30–60 | Charging: 0–45<br>Discharging: −20–60 |
| Storage temperature interval, °C | −20–40 | −20–25 |
| Cell weight, g | 30 g | 40 g |
| Cell size, mm | Height: 65.3 ± 0.1<br>Diameter: 18.4 ± 0.1 | Height: 65.0 ± 0.5<br>Diameter: ≤ 18.6 |

and serial number. For the SIBs, a standard CC-CV charging protocol was applied, wherein the cells were charged at a constant current of 0.5 C to a cutoff voltage of 3.95 V, followed by constant-voltage charging until the current dropped to 65 mA. After a 30-min rest period, the cells were discharged at a constant current of 0.5 C to a cutoff voltage of 1.5 V, with this cycle repeated three times. For the LIBs, a similar CC-CV protocol was employed, charging the cells at a constant current of 0.5 C to a cutoff voltage of 3.65 V, followed by constant-voltage charging until the current decreased to 75 mA. After a 30-min rest, the cells were discharged at a constant current of 0.5 C to a cutoff voltage of 2.0 V, with the cycle also repeated three times. Ultimately, cells with capacity variations within ± 1 % were selected for the experiments.

### 2.2. *Experimental test system*

Fig. 2 illustrates the experimental testbed. In the experimental part of this study, a high-precision battery performance test system (Neware Technology Limited, BTS-60V100A-NTF) was employed to conduct charge/discharge experiments, while a rapid temperature change test chamber (Guangdong Beier, KTBS-1000D-5) provided a constant-temperature environment for the battery. Additionally, a temperature recorder (Keysight Technology, 34970A) was utilized to monitor the surface temperature of the cells via thermocouples. The electrochemical workstation (e DAQ Technology Corporation, ZIVE SP1) was employed for the EIS test, with a frequency range of 0.01–1000 Hz. Fig. 2(b) illustrates the thermal runaway experimental setup. In this study, an external heating methodology was employed for testing, utilizing a silicone rubber heating pad powered by a dedicated heating supply. The heating pad primarily consists of a nickel-chromium alloy heating wire encapsulated within a high-temperature-resistant silicone rubber insulating layer, with a thickness of 1.5 mm, a power rating of 20 W at 24 V, and a heating area of 19 mm × 59 mm. A UNI-T (UTP1310) DC regulated power supply, capable of delivering 32 V/10 A, was employed to energize the heating pad. Temperature monitoring was accomplished by connecting the battery under test to a data logger (HIOKI, LR8400–21) using a K-type thermocouple. Additionally, a high-definition network camera (DS-2DC2402IW-D3/W) was strategically positioned within the laboratory to record the experimental procedures.

Prior to the experiment, all batteries underwent initial capacity testing following the standard test methodology. The standard test conditions were as follows: ambient temperature of 25 °C to 26 °C, charge/discharge rate of 0.5 C, charge cutoff current of 0.05 C, and voltage limits of 3.95 V/1.5 V for SIBs and 3.65 V/2.0 V for LIBs.

### 2.3. *Electrochemical performance testing*

#### 2.3.1. *Impact of ambient temperature on battery capacity*

The ambient temperature was set at 0 °C, 10 °C, 25 °C, and 45 °C. Prior to testing, the batteries were placed in a controlled temperature environment for 3 h to ensure uniform internal and external temperatures of battery. A constant temperature chamber with a fluctuation range of ± 1 °C was used to maintain the desired temperatures

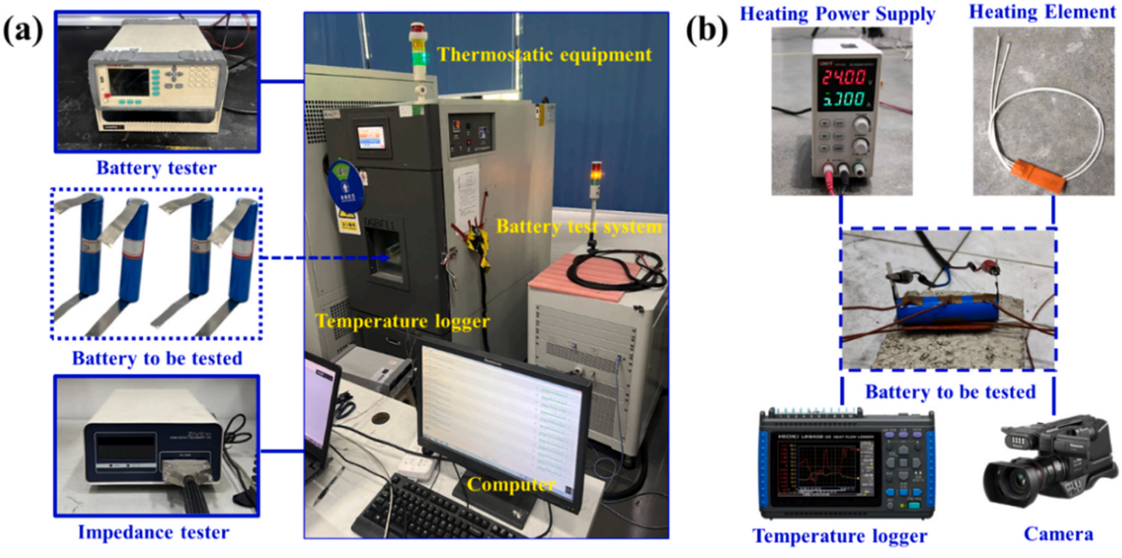

**Fig. 2.** Experimental platforms built: (a) Electrochemical and heat production test and (b) TR test.

throughout the experiment. Standard charging and discharging processes were carried out using the battery performance testing apparatus.

#### 2.3.2. *Impact of rate on battery performance*

Cycling experiments were performed under controlled ambient temperatures ranging from 25 °C to 26 °C. The batteries were charged at a constant rate of 0.5 C and discharged at varying rates (0.5 C, 1 C, 1.5 C, 2 C, and 3 C) for a total of 200 cycles. The ambient temperature was meticulously regulated using an indoor air conditioning system, with fluctuations confined to a narrow range of ± 1°C.

#### 2.3.3. *Impact of overcharging on battery performance*

Three distinct levels of overcharging were applied to the batteries (OB, Overcharged Battery), exceeding the standard charging cutoff voltage by 5 %, 10 %, and 15 %. These results were then compared to those of batteries operating under normal conditions (NB, Normal Battery). Specifically, sodium-ion batteries (SIBs) with a nominal voltage of 3.95 V were charged to 4.2 V, 4.4 V, and 4.6 V, while lithium-ion batteries (LIBs) with a nominal voltage of 3.65 V were charged to 3.8 V, 4.0 V, and 4.2 V. All other experimental conditions, including the standard charging and discharging protocols, remained consistent. Each overcharging cycle consisted of 5 consecutive overcharges, followed by 1 standard charge/discharge cycle.

#### 2.3.4. *Electrochemical impedance spectroscopy (EIS) testing*

The pristine battery, which had not been subjected to any cycling tests, and the battery cycled at the maximum discharge rate (3 C) were stored in a fully discharged state (0 % state of charge, SOC) for over 3 hours under controlled ambient conditions at 25 °C. EIS measurements were subsequently conducted on both batteries, covering a frequency range from 0.01 Hz to 1000 Hz.

### 2.4. *Heat generation characteristic testing*

Heat generation tests were incorporated into both the rate performance and overcharging experiments to comprehensively evaluate thermal behavior. A T-type thermocouple, characterized by a diameter of 1 mm and a measurement range extending from −200 °C to 350 °C, was utilized for precise temperature monitoring. The thermocouple's sensing point was strategically positioned as illustrated in Fig. 3, while the opposing end was interfaced with a high-precision temperature data acquisition system to capture the battery's surface temperature at intervals of one second.

**Fig. 3.** Location of temperature collection points.

### 2.5. *Battery thermal runaway test*

Thermal runaway (TR) experiments were performed on batteries that had undergone maximum overcharging (15 %-OB) and NB, as outlined in Section 2.3. To achieve a SOC of 100 %, the batteries were fully charged at a controlled ambient temperature of 25 °C in accordance with a standardized charging protocol. As illustrated in Fig. 4(b), the battery was heated in an open environment using a silicone rubber heating pad affixed to one side. A K-type thermocouple, with a diameter of 1 mm and a measurement range of −200 °C to 1300 °C, was employed for temperature monitoring. The thermocouple's sensing point was positioned as indicated in Fig. 4(a), while the opposite end was connected to a temperature data acquisition system to record the battery's surface temperature at one-second intervals. The experiment was terminated when the voltage dropped to 0 V following thermal runaway (TR), with data recording continued for an additional 5 min before cessation.

### 2.6. *Battery microstructural characterization*

Disassemble the overcharged batteries within a glove box, ensuring that the batteries are fully discharged to 0 % SOC prior to disassembly. Begin by making several small incisions around the outer ring of the battery's positive terminal, followed by the careful removal of the aluminum casing using sharp-nosed pliers. Meticulously cut through the securing tape to access the internal components. Subsequently, separate the positive and negative electrodes and place them into individual, lidded containers. Add an adequate volume of dimethyl carbonate (DMC) to fully immerse and cleanse the electrodes. After two complete cleaning cycles, dry the components inside the glove box and store them in separate, sealed bags for subsequent analysis. The material on the negative electrode sheet was carefully scraped off using a spatula and ground into a fine powder using a mortar and pestle for microstructural characterization. A section of the negative electrode sheet was excised for detailed surface and cross-sectional microscopic examination. The scanning electron microscopy (SEM) analysis was performed using a Hitachi field emission scanning electron microscope (model SU8010).

Disassemble the overcharged batteries in the glove compartment, ensuring the batteries are at 0 % state of charge prior to disassembly. Initially, create several small incisions in the outer ring of the battery's positive terminal, then utilize sharp-nosed pliers to remove the aluminum casing and meticulously cut through the securing tape. Next, separate the positive and negative electrodes and put them in separate containers with lids. Then, add enough dimethyl carbonate (DMC) to soak and clean the electrodes. After two cleansing cycles, dry the components within a glove box and store them in individual sealed bags for future use. The material on the negative electrode sheet was scraped off with a spatula and ground in a mortar and pestle for micro-characterization of the material. A segment of the negative electrode sheet was extracted for surface and cross-sectional microscopic analysis. The SEM characterization instrument used in this paper is a Hitachi field emission scanning electron microscope (SU8010).

## 3. Results and discussions

### 3.1. *Comparative study of electrochemical performance of SIBs and LIBs*

#### 3.1.1. *Impact of ambient temperature on the performance of SIBs and LIBs*

Fig. 5(a) and (b) illustrate the discharge plateau curves of the batteries under varying ambient temperature conditions. As depicted, both SIBs and LIBs maintain nearly 100 % residual capacity at 25 °C and 45 °C. Specifically, at 45 °C, the capacity retention rates for SIBs and LIBs are 99.90 % and 99.43 %, respectively, whereas at 25 °C, the rates are 98.48 % for SIBs and 99.20 % for LIBs. When the ambient temperature is reduced to 10 °C, the capacity retention rates for SIBs and LIBs decrease to 90.01 % and 90.03 %, respectively. At 0 °C, the capacity

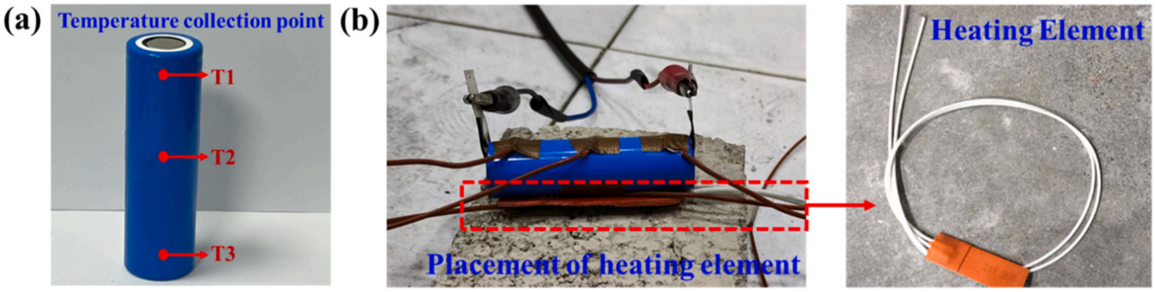

**Fig. 4.** (a) Location of temperature collection points; (b) Placement of heating element.

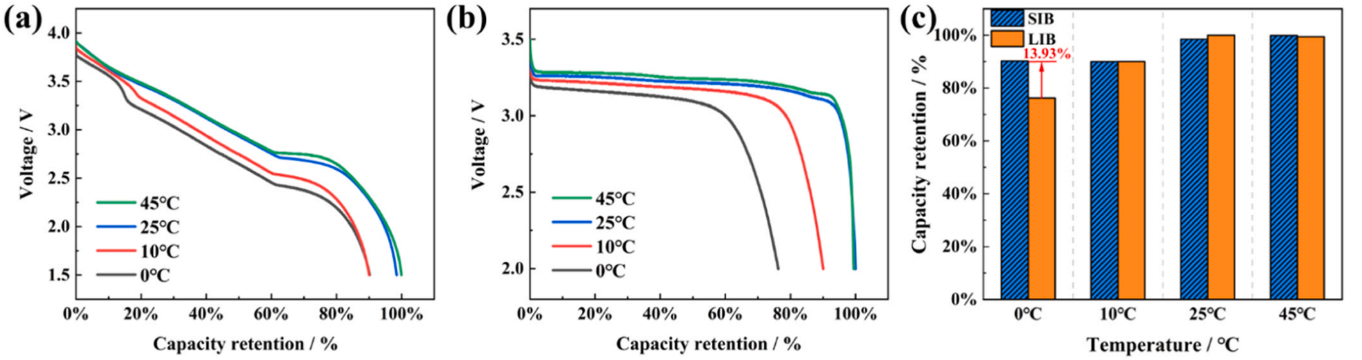

**Fig. 5.** Voltage plateau and capacity changes at various ambient temperatures: (a) SIBs and (b) LIBs discharge plateau curves. (c) A comparison of SIBs and LIBs discharge capacities.

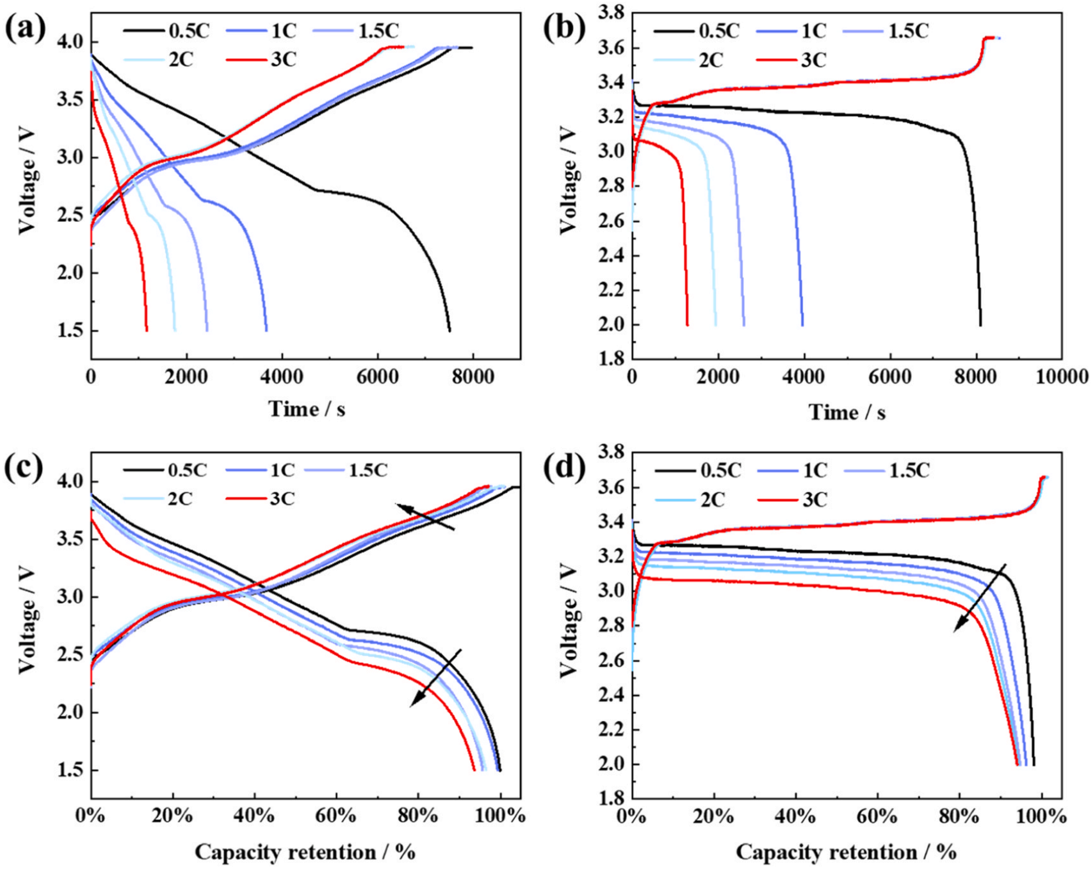

**Fig. 6.** Voltage curve over time of (a) SIBs and (b) LIBs; Capacity retention rate changes of (c) SIBs and (d) LIBs.

retention rates further decline to 90.20 % for SIBs and 76.26 % for LIBs. The discharge plateau progressively diminishes with decreasing ambient temperature, suggesting an increase in the batteries' internal polarization and internal resistance. Although SIBs and LIBs exhibit similar trends, SIBs display superior capacity retention performance at 0 °C compared to LIBs.

The experimental results demonstrate that the discharge capacity of the batteries at 45 °C is marginally higher than that observed at 25 °C. This phenomenon can be explained by the fact that, at 25 °C, the rate of electrochemical reactions within the battery remains moderate, whereas elevated temperatures significantly accelerate these reactions, thereby improving the battery's discharge efficiency. As a result, at 45 °C, the electrochemical reactions within the battery become more pronounced, facilitating the release of a greater amount of energy. When the ambient temperature is reduced to 10 °C, the capacity retention rates of sodium-ion batteries (SIBs) and lithium-ion batteries (LIBs) decrease by 8.47 % and 9.17 %, respectively, relative to their performance at 25 °C. This reduction is primarily caused by the diminished reversibility of active materials, reduced electrolyte activity, and inferior compatibility between the electrolyte and the negative electrode as well as the separator. These factors collectively contribute to an increase in the battery's internal resistance, resulting in a decline in discharge capacity [42]. Under these conditions, SIBs demonstrate a marginally higher discharge capacity compared to LIBs. However, at 0 °C, as depicted in Fig. 3(C), the capacity retention rate of SIBs is 13.93 % higher than that of LIBs. This enhanced performance is attributed to the superior low-temperature properties of the electrolyte employed in SIBs. Specifically, the electrolyte in sodium-ion batteries exhibits better fluidity at low temperatures compared to that in lithium-ion batteries, thereby promoting faster diffusion of sodium ions within the electrolyte [43].

### 3.1.2. *Impact of different discharge rates on the performance of SIBs and LIBs*

The discharge characteristics of batteries under varying discharge rates at an ambient temperature of 25 °C are illustrated in Fig. 6. Specifically, Fig. 6(a) and (b) present the discharge voltage profiles as a function of time, while Fig. 6(c) and (d) demonstrate the relationship between discharge capacity and capacity retention rates. The experimental data reveal that at discharge rates of 0.5 C, 1 C, 1.5 C, 2 C, and 3.0 C, the discharge durations for SIBs are 7505 s, 3671 s, 2430 s, 1756 s, and 1162 s, respectively. In contrast, for LIBs, the corresponding durations are 8104 s, 3960 s, 2596 s, 1938 s, and 1288 s. The results demonstrate that an increase in discharge rate leads to a decline in the discharge plateau and a significant reduction in discharge duration. During the later stages of discharge, a sharp voltage drop is observed, primarily attributable to intensified polarization effects. At this stage, the polarization within the battery increases substantially, resulting in a marked rise in internal resistance and a consequent rapid decrease in voltage. Additionally, higher discharge currents exacerbate the voltage drop across the internal resistance, leading to lower terminal voltages [44]. Furthermore, as depicted in Fig. 6(c) and (d), the discharge capacity exhibits a gradual decline with increasing discharge rates. At 0.5 C, 1 C, 1.5 C, 2 C, and 3.0 C, the capacity retention rates for SIBs are 100.00 %, 100.00 %, 95.64 %, 96.44 %, and 93.60 %, respectively, whereas for LIBs, the rates are 98.10 %, 96.20 %, 94.72 %, 94.32 %, and 94.02 %. This phenomenon arises from the increased voltage drop caused by internal resistance at higher discharge rates, which limits the participation of active materials in electrochemical reactions before the cutoff voltage is reached, thereby reducing the overall discharge capacity. Moreover, the Joule heat generated during high-rate discharge induces a temperature rise within the battery, potentially initiating side reactions or accelerating material degradation, which further compromises capacity retention [45].

### 3.1.3. *Impact of cycle number on the capacity retention of SIBs and LIBs*

The capacity retention rates of batteries under varying discharge rates, plotted as a function of cycle number, are depicted in Fig. 7. At discharge rates of 0.5 C, 1 C, 1.5 C, 2 C, and 3 C, the capacity retention rates for SIBs are 97.51 %, 93.45 %, 90.29 %, 85.44 %, and 79.28 %, respectively. In comparison, LIBs exhibit capacity retention rates of 97.63 %, 96.66 %, 96.18 %, 94.53 %, and 95.09 % under the same conditions. The experimental findings demonstrate that battery degradation is exacerbated with increasing discharge rates. This phenomenon is primarily attributed to the substantial increase in current density at higher discharge rates, which induces excessive heat generation, thereby triggering electrolyte decomposition, electrode material degradation, and ultimately a progressive decline in battery capacity. Moreover, SIBs display a more pronounced degradation rate compared to LIBs. This disparity arises from the larger ionic radius of $Na^+$ relative to $Li^+$, which imposes greater mechanical strain during the intercalation and deintercalation processes. Such strain facilitates cathode material cracking and anode material structural instability, leading to accelerated deterioration of the battery's internal structure and a consequent reduction in its operational lifespan [37]. For LIBs, the rate of capacity decay increases progressively with higher charge/discharge rates, ranging from 0.5 C to 2 C. In contrast, during the initial stages of cycling at 3 C, the capacity decay rate is relatively slower but accelerates significantly in the later stages. Previous studies have indicated that the capacity decay of batteries tends to decelerate in the later stages when cycled at higher charge/discharge rates, a phenomenon that is corroborated by the current experimental results.

### 3.1.4. *Comparison of AC impedance between SIBs and LIBs*

Fig. 8 displays the EIS curves for both the pristine battery and the battery cycled at a 3 C rate. As illustrated in the figure, the impedance of the battery following 3 C cycling is markedly higher than that of the pristine battery, suggesting that a significant increase in resistance is one of the key factors contributing to battery degradation after high-rate

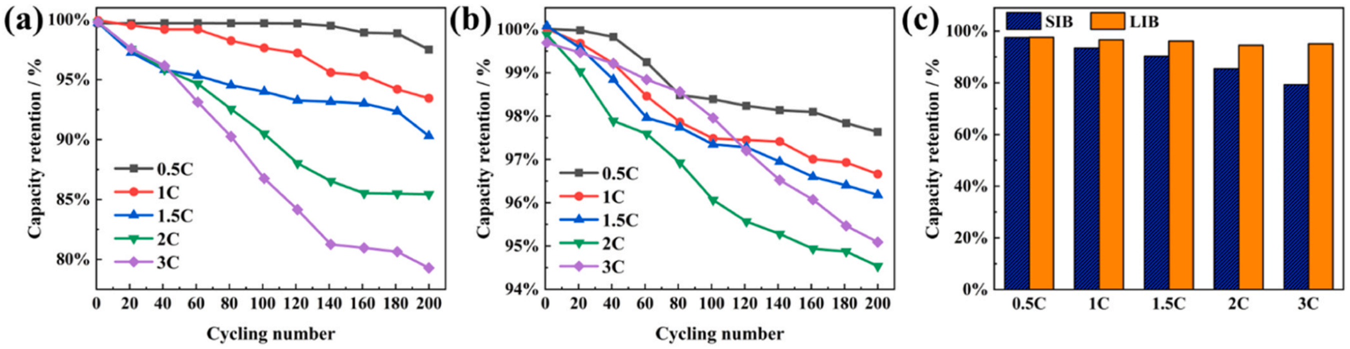

**Fig. 7.** Changes in battery capacity retention following cycling at various multiplicities: (a) SIBs, (b) LIBs and (c) A comparison of the final capacity retention of SIBs and LIBs.

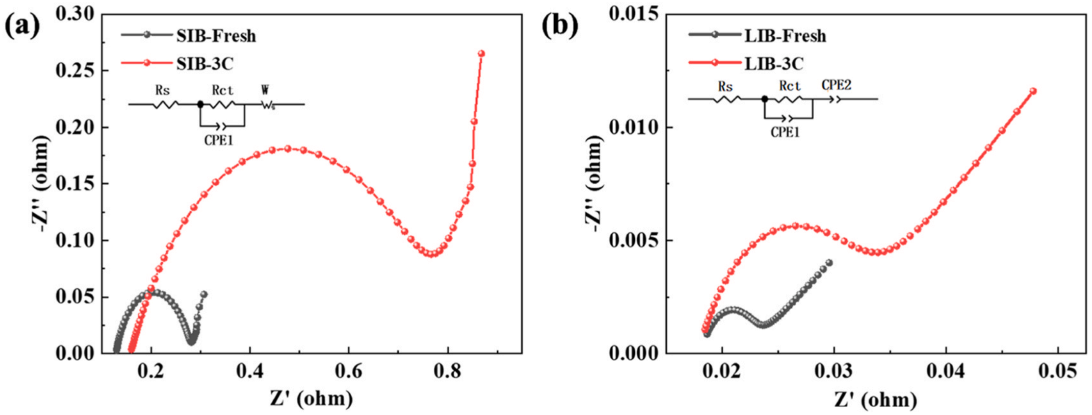

**Fig. 8.** EIS curves of new cells versus cells after 3 C cycles (a) SIBs and (b) LIBs.

charge/discharge cycles. The ohmic resistance ($R_{oh}$), determined by the intersection of the curve with the real axis, exhibits a noticeable increase for SIB, rising from 0.1286 Ω to 0.1578 Ω, while the change in ohmic resistance for LIB remains minimal. The charge transfer resistance ($R_{ct}$), represented by the diameter of the semicircle in the medium-to-high frequency region, corresponds to the resistance associated with electrochemical reactions during charge transfer. Both LIB and SIB demonstrate a substantial rise in $R_{ct}$, with LIBs increasing from 0.0042 Ω to 0.1238 Ω and SIB increasing from 0.1511 Ω to 0.6180 Ω. This observation implies that the charge transfer resistance progressively increases during battery cycling. The linear segment in the low-frequency region of the EIS curve signifies the solid-phase diffusion resistance of $Na^+$ and $Li^+$ within the electrode active materials. The steeper slope of this line after 3 C cycling indicates an incremental rise in solid-phase diffusion resistance during battery cycling. Detailed quantitative data are summarized in Table 2.

### 3.1.5. *The impact of overcharge level on the performance of SIBs and LIBs*

The overcharging levels were set at 5 %, 10 %, and 15 %. For LIBs, the NB voltage was 3.65 V, with overcharging voltages of 3.8 V (5 %), 4.0 V (10 %), and 4.2 V (15 %). For SIBs, the NB voltage was 3.95 V, with overcharging voltages of 4.2 V (5 %), 4.4 V (10 %), and 4.6 V (15 %). To evaluate the residual capacity at different stages, a standardized capacity test was performed after every five overcharge cycles, and the results are presented in Fig. 9. After multiple overcharge cycles, the residual capacities of all overcharged batteries showed premature degradation compared to the NB. For LIBs, the residual capacities of the NB and OB at 5 %, 10 %, and 15 % overcharging were 98.97 %, 98.89 %, 98.86 %, and 99.07 %, respectively. For SIBs, the residual capacities of the NB and OB at 5 %, 10 %, and 15 % overcharging were 99.70 %, 97.65 %, 92.08 %, and 67.72 %, respectively. The data indicate that as the degree of overcharging increases, the capacity retention rates of both SIBs and LIBs progressively decrease, with the rate of decline accelerating. Notably, SIBs exhibit a significantly faster degradation rate compared to LIBs. Based on the final capacity test, Fig. 9(c) illustrates the residual capacities of SIBs and LIBs after mild overcharge cycling. As depicted in the figure, the residual capacities of SIBs at all overcharging levels are consistently lower than those of LIBs. For LIBs, the differences in residual capacities between the overcharged batteries and the NB are 0.09 %, 0.11 %, and 0.10 %, respectively, indicating minimal variations. This suggests that the overcharge cycles in this study had a negligible impact on the performance of LIBs. In contrast, for SIBs, the differences in residual capacities between the overcharged batteries and the NB are 2.05 %, 7.62 %, and 31.98 %, respectively. Particularly, under the maximum overcharging level (15 %), the overall capacity decay of SIBs shows a rapid decline, with a capacity retention rate 33.35 % lower than that of LIBs. This accelerated degradation may be due to more severe electrochemical side reactions, such as electrolyte decomposition and thickening of the solid electrolyte interphase layer, which deplete sodium ions and reduce the availability of active materials for charge/discharge processes. These findings demonstrate that LIBs exhibit superior cycle stability compared to SIBs under mild overcharging conditions.

**Table 2**
Impedance fitting results.

| Items | $R_{oh}/\Omega$ | $R_{ct}/\Omega$ |
|---|---|---|
| SIB-Fresh | 0.1286 | 0.1511 |
| SIB-3C | 0.1578 | 0.6180 |
| LIB-Fresh | 0.0180 | 0.0042 |
| LIB-3C | 0.0176 | 0.1238 |

## 3.2. *Heat generation characteristics of SIBs and LIBs*

### 3.2.1. *Comparison of heat generation in batteries at different discharge rates*

The batteries were discharged at rates of 0.5 C, 1 C, 1.5 C, 2 C, and 3 C in a constant temperature chamber maintained at 25 °C. During the discharge process, the surface temperatures of the batteries were monitored over time, as depicted in Fig. 10. The results indicate that the peak surface temperature during discharge increases with higher discharge rates. For LIBs, the peak temperatures recorded at these discharge rates were 27.65 °C, 29.84 °C, 31.56 °C, 33.12 °C, and 36.45 °C, respectively. In comparison, SIBs exhibited peak temperatures of 27.67 °C, 29.41 °C, 30.82 °C, 30.46 °C, and 33.27 °C under identical conditions. Fig. 10(c) illustrates the maximum temperature differentials between the discharge temperature and the initial temperature. For LIBs, these differentials were 1.56 °C, 3.81 °C, 5.50 °C, 7.02 °C, and 10.29 °C, while for SIBs, they were 1.94 °C, 3.42 °C, 4.83 °C, 4.68 °C, and 7.61 °C. The analysis reveals that at a discharge rate of 0.5 C, LIBs exhibited a slightly lower peak surface temperature than SIBs. However, at higher discharge rates (1 C, 1.5 C, 2 C, and 3 C), LIBs consistently demonstrated higher peak surface temperatures compared to SIBs, with the temperature disparity progressively increasing to 0.387 °C, 0.675 °C, 2.341 °C, and 2.683 °C, respectively.

The temperature rise curves demonstrate that higher discharge currents result in both higher and faster temperature increases. During the initial stage of battery discharge, the temperature rises rapidly. In the intermediate stage, the temperature increase becomes relatively gradual. Subsequently, the battery temperature experiences another rapid rise. This trend is particularly pronounced at a discharge rate of 0.5 C. This phenomenon is primarily attributed to the following underlying mechanisms: During the initial phase of discharge, the rapid escalation in battery temperature is predominantly driven by two critical factors. Firstly, the minimal thermal gradient between the battery

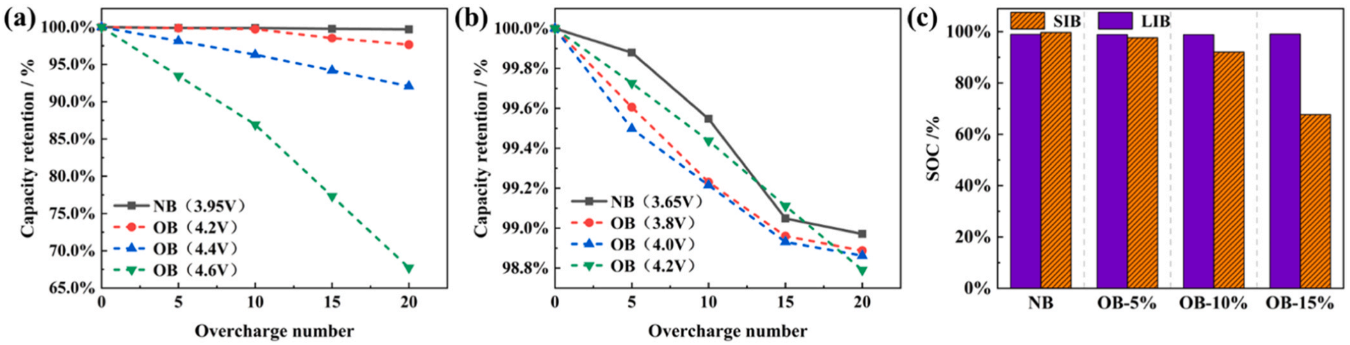

**Fig. 9.** Battery capacity degradation curves: (a) SIBs, (b) LIBs and (c) Comparing capacity retention after overcharging between SIBs and LIBs.

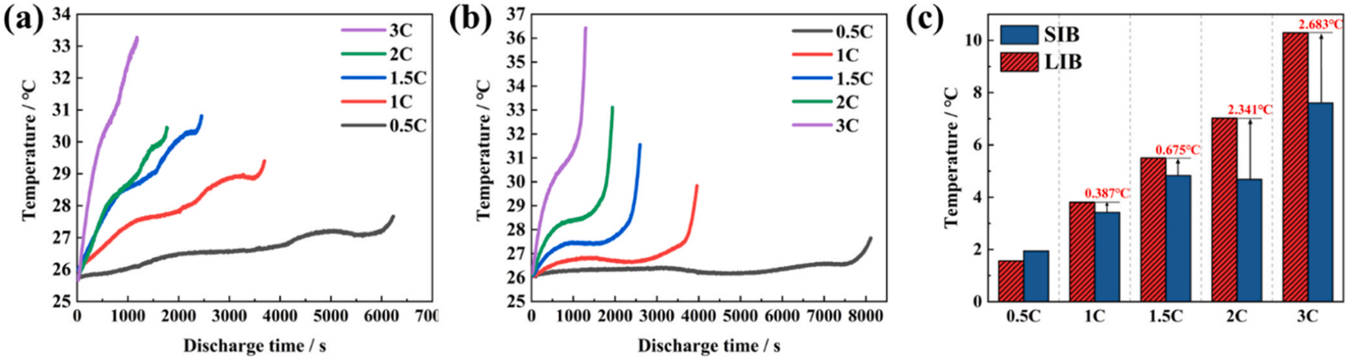

**Fig. 10.** Variation of cell surface temperature throughout discharge time: (a) SIBs; (b) LIBs; (c) Comparison of maximum temperature rise between SIBs and LIBs at various multiplicities.

and its ambient environment results in diminished heat exchange efficiency, thereby impeding the rate of thermal dissipation. Secondly, the elevated activation energy required for internal electrochemical reactions, combined with the pronounced Joule heating effect induced by ohmic resistance and electrochemical polarization, culminates in a heat generation rate that surpasses the rate of heat dissipation. As the discharge process progresses, the battery transitions into a phase characterized by a moderated temperature increase. This stage is distinguished by an augmented thermal gradient between the battery's core and the external environment, significantly enhancing the efficiency of heat dissipation. Concurrently, the concentration gradient of active materials within the battery stabilizes, and the extent of electrochemical polarization remains relatively invariant, ensuring a consistent heat generation rate. At this juncture, the thermal equilibrium state of the battery system precipitates a marked deceleration in the rate of temperature rise. In the terminal phase of discharge, the rate of temperature increase undergoes a pronounced acceleration, a consequence of the synergistic interplay of multiple contributing factors. Primarily, the substantial reduction in electrolyte concentration within the battery augments ionic migration resistance, leading to intensified ohmic polarization. Additionally, the precipitous decline in the concentration of active materials at the electrode surfaces exacerbates concentration polarization. Ultimately, the internal resistance of the battery experiences a significant surge with increasing discharge depth. These factors collectively engender a dramatic amplification of the Joule heating effect, precipitating a substantial escalation in the heat generation rate, which is ultimately manifested as a rapid ascent in the rate of temperature increase.

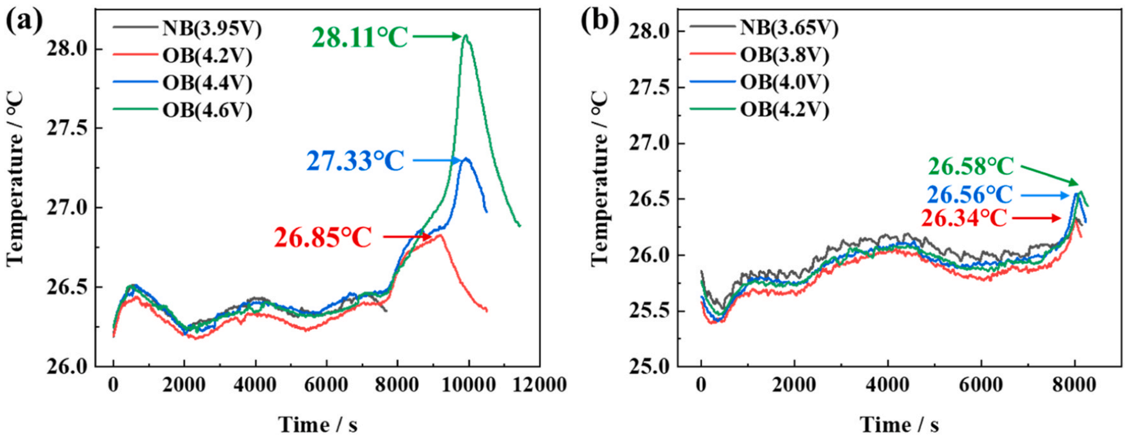

**Fig. 11.** The surface temperature of the battery is measured at various degrees of overcharge: (a) SIBs and (b) LIBs.

### *3.2.2. Comparison of heat generation in batteries with different degrees of overcharge*

The surface temperature of the batteries was monitored during both normal charging and overcharging processes (5 %, 10 %, and 15 %), with the resulting temperature profiles depicted in Fig. 11. The data reveal that the peak surface temperature of the batteries increases with the degree of overcharging. For LIBs, under normal charging conditions, the peak surface temperature was recorded at 26.36 °C. In contrast, under overcharging conditions of 5 %, 10 %, and 15 %, the peak temperatures were 26.34 °C, 26.56 °C, and 26.58 °C, respectively. On the other hand, SIBs exhibited a peak surface temperature of 26.54 °C under normal charging, which increased to 26.85 °C, 27.33 °C, and 28.11 °C under overcharging conditions of 5 %, 10 %, and 15 %, respectively. Notably, the peak surface temperatures of SIBs were consistently higher than those of LIBs across all overcharging levels, with temperature differences of 0.51 °C, 0.77 °C, and 1.53 °C, respectively.

Figs. 12 and 13 depict the initial charging process of SIBs and LIBs, as well as the temperature rise caused by various levels of overcharging. During the initial stage of constant-current charging, the rapid extraction of ions from the cathode and their subsequent insertion into the anode, coupled with the combined effects of reaction heat, ohmic heat, and polarization heat, results in a significant temperature rise due to the relatively high internal resistance of the battery. In the intermediate charging phase, as the extraction and insertion of ions in the cathode and anode materials approach saturation, the rate of electrochemical reactions begins to decelerate, leading to a reduction in heat generation. Consequently, the surface temperature of the battery decreases and stabilizes. During the final charging stage, excessive extraction of ions from the cathode material induces irreversible structural changes, while metallic deposition occurs at the anode. These processes are accompanied by substantial energy dissipation and heat release, causing a rapid increase in the battery's surface temperature. When the voltage exceeds the standard cut-off voltage, all batteries with varying degrees of overcharge reach their maximum temperature. However, if charging continues beyond this point, the battery's surface temperature slightly decreases. This phenomenon occurs because, when a battery is fully charged, the internal electrochemical reactions become saturated, leading to minimal heat generation. According to existing literature, the entropy heat coefficient of a battery initially increases and then decreases as the state of charge (SOC) rises. As the SOC approaches 100 %, the entropy heat coefficient becomes negative, indicating that the reaction heat enters an endothermic state. When the absolute value of the negative reversible heat exceeds the irreversible heat, the overall heat generation of the battery turns negative, causing a temperature drop. Furthermore, the precision and sensitivity of the testing equipment significantly influence the experimental outcomes. As illustrated in Fig. 11(b), during the initial phase of the charging process, the surface temperature of the battery exhibited a decline due to the thermal inertia of the constant temperature chamber, which led to an unstable initial temperature. Subsequently, the temperature increased as the heat generated by the charging process accumulated. Therefore, in practical applications, the surface temperature of the battery can only serve as one of the monitoring parameters and is insufficient as a standalone indicator to determine whether the battery is in an overcharged state.

### *3.3. TR characteristics evaluation of overcharged batteries*

Tests were conducted using batteries that had undergone cycling at the maximum overcharge level (15 %). Fig. 14 presents the temperature and voltage profiles over time during the thermal runaway test. The data reveal that under identical heating conditions, the SIB experienced thermal runaway, whereas the LIB did not. As shown in Fig. 14, the

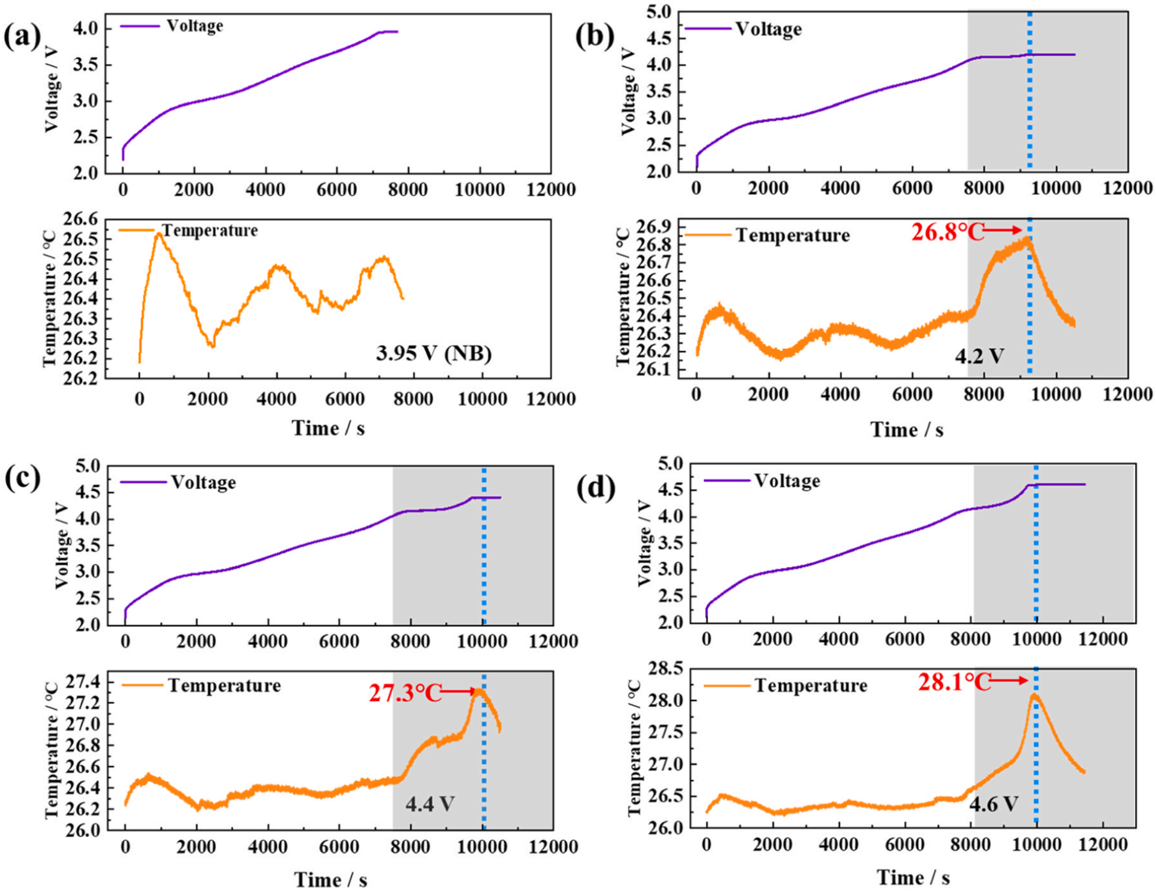

**Fig. 12.** SIBs charging voltage and surface temperature variation curves: (a) NB, (b) OB-4.2 V, (c) OB-4.4 V, and (d) OB-4.6 V.

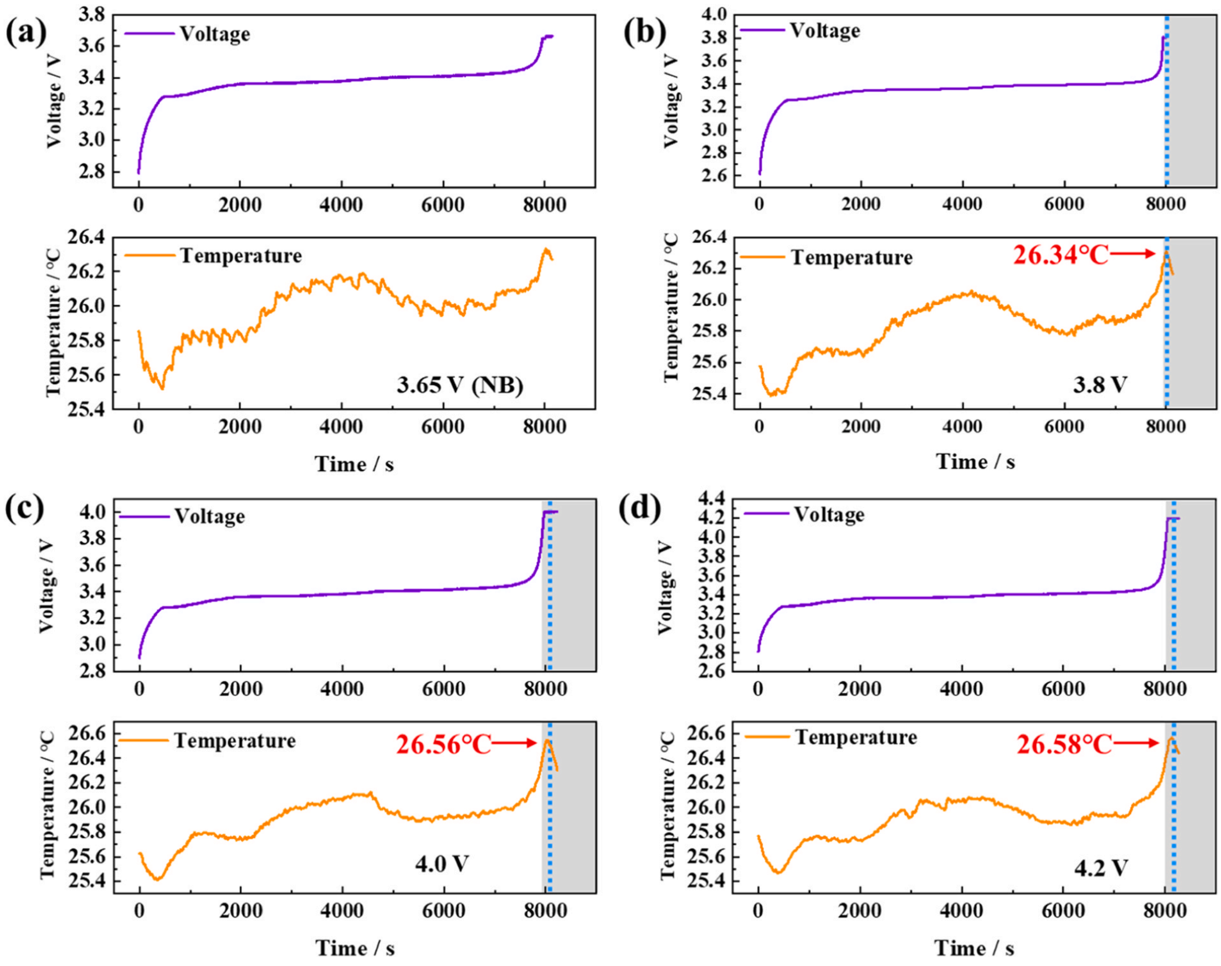

**Fig. 13.** LIBs charging voltage and surface temperature variation curves: (a) NB, (b) OB-3.8 V, (c) OB-4.0 V, and (d) OB-4.2 V.

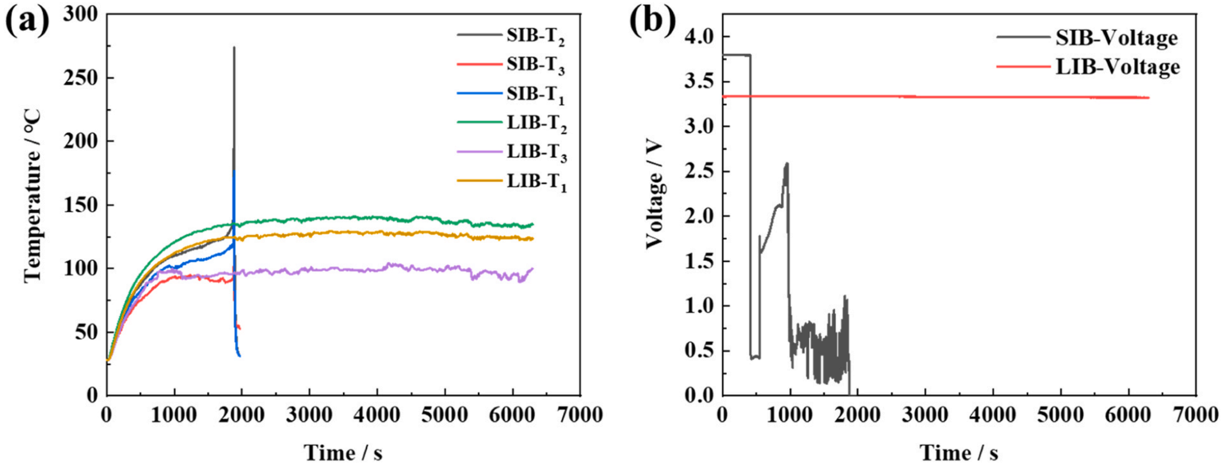

**Fig. 14.** (a) Temperature at different regions on the surface of SIBs and LIBs; (b) Voltage variations of SIBs and LIBs.

voltage of the SIB abruptly dropped to 0.53 V when the temperature at monitoring point $T_2$ reached 81.6 °C, and it remained at this level for approximately 135 s. When $T_2$ further increased to 194.6 °C, the voltage of the SIB dropped to 0 V. During the thermal runaway process of the SIB, the peak temperature at $T_2$ reached 273.9 °C, while $T_3$ and $T_1$ recorded temperatures of 102 °C and 171.7 °C, respectively. In contrast, the LIB did not exhibit thermal runaway during the experiment, with its maximum temperature reaching 140°C and the voltage remaining stable around 3.3 V without significant fluctuations. As discussed in Section 3.1.5, the SOC of the SIB at the maximum overcharge level (15 %) was 67 %, significantly lower than the 80 % threshold, whereas the LIB maintained a healthy SOC of 98.79 %. Additionally, as highlighted in Section 3.2.2, under overcharge abuse conditions, the surface temperature of SIBs was higher than that of LIBs, indicating an increase in internal resistance and polarization within the SIBs. This inherent instability under overcharge conditions makes thermal runaway an inevitable outcome for SIBs. These findings further corroborate that SIBs exhibit inferior stability compared to LIBs under overcharge abuse and pose significant thermal safety risks.

Fig. 15 illustrates the changes in the appearance and morphology of the two battery types before and after the TR test, corroborating the findings discussed above. The surface of the SIB exhibited clear signs of combustion, with visible damage to both the cathode and anode. In contrast, the LIB did not undergo thermal runaway, and its surface remained intact without any noticeable deterioration. These observations align with the experimental data presented earlier.

### *3.4. Macrostructure of battery anode and cathode*

The batteries subjected to varying degrees of overcharging were disassembled, and their electrodes were examined, as illustrated in Fig. 16. It is evident that the morphology of both the positive and negative electrodes of the LIBs remained largely intact without significant damage. Similarly, the positive electrodes of the SIBs also showed no apparent deterioration. However, the negative electrodes of the SIBs exhibited increasingly severe damage as the degree of overcharging intensified. When the negative electrodes of the SIBs were unfolded, rapid heat generation was observed, accompanied by significant delamination of the active material. The surface appeared whitened and became soft and fragile, a phenomenon likely attributed to sodium deposition reactions occurring on the negative electrodes. Sodium deposition reactions typically occur at the negative electrode of SIBs.

Upon disassembly of the battery, it was observed that no significant alterations had occurred in the cathodes. Consequently, SEM analysis was exclusively conducted on the anode. Fig. 17 illustrates the microscopic morphologies of the anode electrode's cross-sections and surfaces. Fig. 17(a)–(d) and Fig. 17(i)–(l) depict the cross-sectional morphologies of the anode electrodes of LIBs and SIBs, respectively. As shown in the images, the active materials at the cross-sections of NB for both types of batteries are securely and uniformly packed, with no delamination. For OB-5 %, minor cracks form in the active material layer at the cross-section, along with slight separation from the current collector. With OB-10 %, cross-sectional delamination worsens, accompanied by mild shedding and collapse of the active material. At OB-15 %, delamination is most severe, with active materials spread unevenly, significant powder loss, and structural collapse. Fig. 17(e) to (h) illustrate the surface morphologies of the LIBs anode electrodes. The NB exhibits a smooth and homogeneous surface, as indicated in the images. Cracks form in the surface active materials of OB-5 % and OB-10 %. When the battery is OB-15 %, the surface active materials shed off, exposing the current collector. This results in a reduction in the quantity of active materials and a corresponding drop in battery capacity, supporting the conclusion established in Section 3.1.5 that the greater the degree of overcharge in LIBs, the larger the capacity fade. Furthermore, if active materials fall into the electrolyte, they can increase the internal resistance of the battery or potentially cause battery damage, posing a safety risk. Fig. 17(m)–(p) show the surface morphologies of the SIBs anode electrodes. As illustrated in the images, the NB's surface material is densely packed and homogeneous, with distinct boundaries between material particles. In overcharged batteries with OB-5 %, OB-10 %, and OB-15 %, the boundaries of the active components become increasingly blurred and fused.

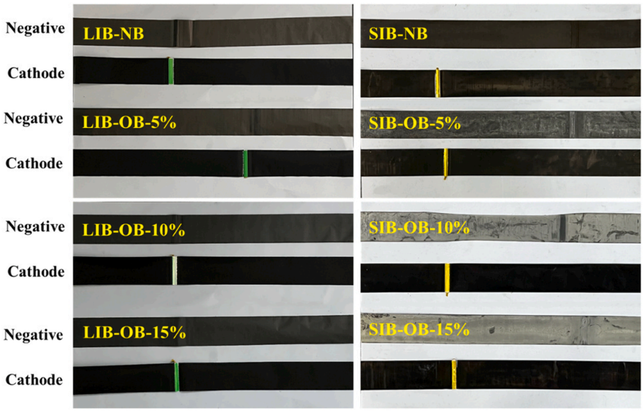

**Fig. 16.** Different overcharge levels of electrode morphology of LIBs and SIBs.

The microscopic morphologies of the battery anode materials are displayed in Fig. 18. The microscopic morphologies of the LIBs anode active materials are compared in Fig. 18(a)–(d). As depicted in the images, the active material particles in the NB exhibit uniform sizes and distinct boundaries. In the case of OB-5 %, the particles agglomerate, and the anode active materials become rougher. At OB-10 %, slight agglomeration of the materials is observed, along with increased roughness in the anode active materials and blurred, disordered particle gaps. In the battery with OB-15 %, agglomeration and fractured anode active material particles are evident. Overcharging cycles lead to excessive lithium intercalation in the anode material over time, resulting in volume expansion and increased interlayer gaps. When the internal stress within the anode active material exceeds its mechanical stability limit, it causes structural breakage, agglomeration, and material shedding [46].

Fig. 18(e) to (h) illustrate the morphologies of the SIBs anode active materials. As shown in the images, the active material particles in the NB are evenly sized and have distinct boundaries. In the case of OB-5 %,

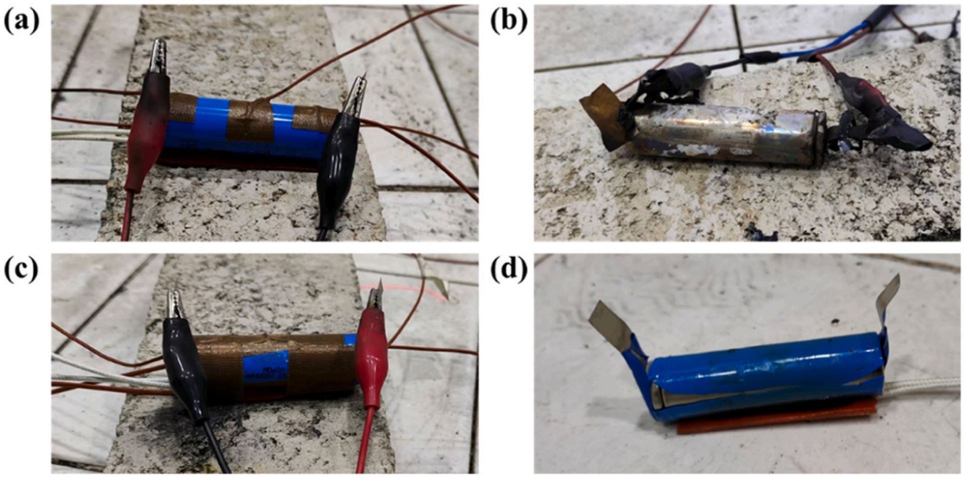

**Fig. 15.** Battery morphology before and after TR testing: (a) Before testing of SIBs; (b) After testing of SIBs; (c) Before testing of LIBs; (d) After testing of LIBs.

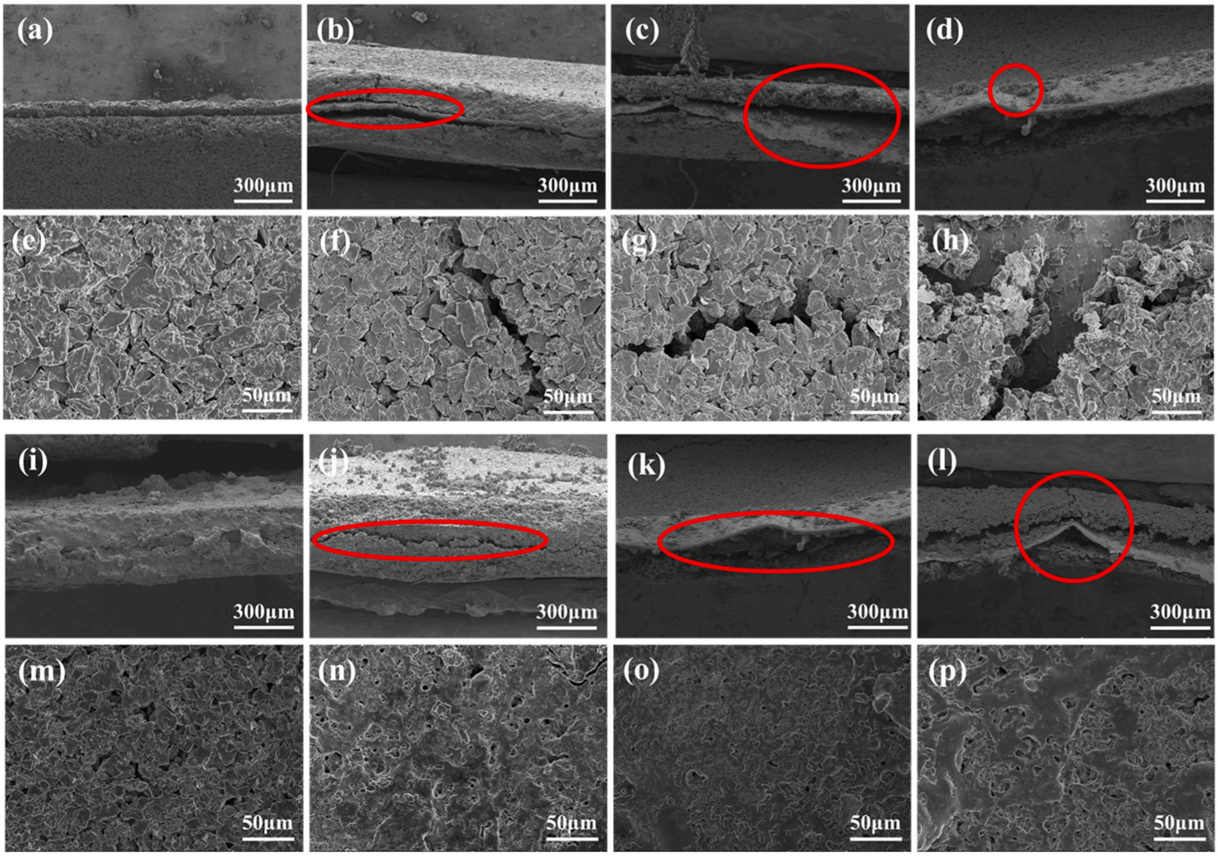

**Fig. 17.** Cross-sectional SEM morphology of negative electrode sheet of overcharged battery: LIB-NB~OB-15 %: (a)–(d) ; SIB-NB~OB-15 %:(i)–(l) ; SEM morphology of negative electrode surface of overcharged batteries: LIB-NB~OB-15 %: (e)–(h) ; SIB-NB~OB-15 %: (m)–(p) ; .

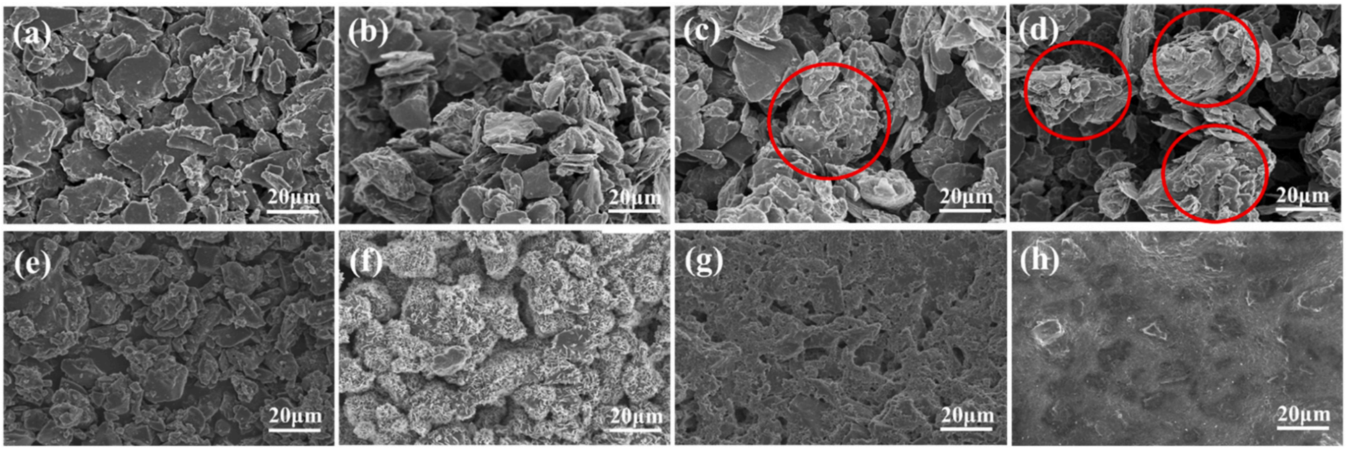

**Fig. 18.** SEM of the anode material: (a) LIB-NB, (b) LIB-OB-5 %, (c) LIB-OB-10 % and (d) LIB-OB-15 %; (e) SIB-NB, (f) SIB-OB-5 %, (g) SIB-OB-10 % and (h) SIB-OB-15 %.

sodium clusters form, followed by the deposition of sodium dendrites [47,48]. For OB-10 % and OB-15 %, the sodium clusters on the surface dissolve, and bulk materials emerge. Due to the substantial amount of sodium plating, the anode surface is almost entirely covered by these bulk materials. In the OB-15 % case, the surface is fully covered with metallic sodium. This indicates that repeated overcharging causes irregular deposition of sodium ions, leading to the formation of "inactive sodium" or sodium dendrites. This phenomenon reduces the Coulombic efficiency, resulting in rapid capacity fading. These observations help explain the significant capacity fading observed in the SIB-OB-15 % scenario described in Section 3.1.5.

## 4. Conclusion and outlook

### 4.1. Conclusion

Comparative studies were conducted between LIBs and SIBs by varying ambient temperature, charge/discharge rates, and overcharging levels to systematically evaluate and analyze their electrochemical performance and thermal behavior. The fundamental causes of the observed performance degradation were elucidated from a microscopic perspective.

The key findings are as follows:

(1) At 0 °C, SIBs demonstrate a higher discharge capacity compared to LIBs. At 45 °C, 25 °C, and 10 °C, the 0.5 C discharge capacities of SIBs and LIBs differ by 0.5–0.8 %. Notably, at 0 °C, the 0.5 C discharge capacity of SIBs is 13.93 % higher than that of LIBs. However, after high-rate (3 C) cycling at 25 °C, the capacity of SIBs declines more rapidly than that of LIBs. Ultimately, the capacity retention rate of SIBs is 15.81 % lower than that of LIBs.

(2) SIBs exhibit greater safety under normal operating conditions but demonstrate inferior thermal stability under abusive conditions. Under normal working conditions at the maximum discharge rate (3 C), SIBs generate less surface heat than LIBs, with a difference of 2.683 °C. However, under the maximum overcharging level (15 %) in abusive conditions, SIBs produce more surface heat than LIBs, with a difference of 1.53 °C. Additionally, SIBs are more prone to thermal runaway than LIBs after overcharging, reaching a maximum thermal runaway temperature of 273.9 °C.

(3) The microanalysis aligns with the macro test data, revealing that the significant decline in SIB performance and poor thermal stability under abusive conditions are primarily due to severe sodium deposition reactions on the negative electrode and substantial shedding of active materials. These phenomena lead to reduced charging and discharging efficiency and increased heat generation due to elevated internal resistance.

### *4.2. Outlook*

This thesis investigates the fundamental thermal-electrical characteristics of SIBs and LIBs at both macro and micro levels, including their thermal runaway behavior and the underlying mechanisms of performance degradation under overcharge abuse. However, significant work remains to be addressed in future studies, as outlined below:

(1) The research in this thesis focuses on 18650 cylindrical cells, without addressing large-capacity soft-pack or prismatic cells. Future work should extend to large-capacity, high-energy-density, and large-format batteries, aligning with the current development trends in power and electrochemical energy storage. Additionally, efforts should be made to enhance the intrinsic, active, and passive safety of SIBs through a material-cell-module system approach.

(2) The performance of SIBs and LIBs can be improved by optimizing electrode materials, enhancing the stability of cell interfaces through surface modification, interfacial coating, or interfacial modulation, and optimizing current collectors and binders. This includes selecting more compatible current collector materials and binders with higher bond strength and stability.

(3) While this thesis employs experimental methods to study the thermal safety of SIBs, future research should integrate simulation techniques to analyze temperature distribution under normal use, abuse conditions, and thermal runaway propagation. This will help in understanding and controlling the maximum temperature values and temperature uniformity to improve safety.

## CRediT authorship contribution statement

**Jiangyun Zhang:** Writing – review & editing, Supervision, Funding acquisition. **Jiantao Zhang:** Resources, Investigation. **Guoqing Zhang:** Supervision, Resources, Funding acquisition. **Han Xu:** Writing – review & editing, Writing – original draft, Investigation. **Liqin Jiang:** Resources. **Hongwei Wu:** Resources. **Wenzhao Jiang:** Resources. **Kang Peng:** Resources. **Jun Liu:** Resources.

## Declaration of Competing Interest

The authors declare that they have no known competing financial interests or personal relationships that could have appeared to influence the work reported in this paper.

## Acknowledgements

This research was financially supported by Major Science and Technology Project in Dongguan (20231200300022), Science and Technology Project of Guangdong Administration for Market Regulation (2023ZZ06, 2024CZ08), Zhuhai Science and Technology Planning Project in the Field of Social Development (2420004000156).

## References

[1] Y. Miao, P. Hynan, A. von Jouanne, A. Yokochi, Current li-ion battery technologies in electric vehicles and opportunities for advancements, Energies 12 (6) (2019) 1074, https://doi.org/10.3390/en12061074.

[2] C.P. Zhao, J.H. Sun, Q.S. Wang, Thermal runaway hazards investigation on 18650 lithium-ion battery using extended volume accelerating rate calorimeter, J. Energy Storage 28 (2020) 101232, https://doi.org/10.1016/j.est.2020.101232.

[3] Y. Cui, J.H. Lui, Research progress of water mist fire extinguishing technology and its application in battery fires, Process Saf. Environ. Prot. 149 (2021) 559–574, https://doi.org/10.1016/j.psep.2021.03.003.

[4] X.Y. Tang, Q.R. Jia, L.Y. Yang, et al., Towards the high-energy-density battery with broader temperature adaptability: self-discharge mitigation of quaternary nickel-rich cathode, Energy Storage Mater. 33 (2020) 239–249, https://doi.org/10.1016/j.ensm.2020.08.020.

[5] W.J. Choi, D. Aurbach, Promise and reality of post-lithium-ion batteries with high energy densities, Nat. Rev. Mater. 1 (4) (2016) 359–367, https://doi.org/10.1038/natrevmats.2016.13.

[6] X.Q. Zeng, M. Li, D. Abd El-Hady, et al., Commercialization of lithium battery technologies for electric vehicles, Adv. Energy Mater. 9 (27) (2019), https://doi.org/10.1002/aenm.201900161.

[7] R. Liu, B. Zhang, L. Fu, et al., Classification, fabrication, and modification of carbon spheres for sodium-ion batteries, Mater. Today Chem. 35 (2024) 101903, https://doi.org/10.1016/j.mtchem.2024.101903.

[8] R.Q. Peng, D.P. Kong, P. Ping, et al., Thermal runaway modeling of lithium-ion batteries at different scales: recent advances and perspectives, Energy Storage Mater. 69 (2024) 103417, https://doi.org/10.1016/j.ensm.2024.103417.

[9] P.F. Huang, P. Ping, K. Li, et al., Experimental and modeling analysis of thermal runaway propagation over the large format energy storage battery module with $Li_4Ti_5O_{12}$ anode, Appl. Energy 183 (2016) 659–673, https://doi.org/10.1016/j.apenergy.2016.08.160.

[10] O.A. Said, C. Lee, S.I. Stoliarov, Experimental investigation of cascading failure in 18650 lithium-ion cell arrays: impact of cathode chemistry, J. Power Sources 446 (2020) 227347, https://doi.org/10.1016/j.jpowsour.2019.227347.

[11] S. Gao, X.N. Feng, L. Lu, et al., An experimental and analytical study of thermal runaway propagation in a large format lithium-ion battery module with NCM pouch-cells in parallel, Int. J. Heat Mass Transf. 135 (2019) 93–103, https://doi.org/10.1016/j.ijheatmasstransfer.2019.01.125.

[12] T.F. Gao, Z.R. Wang, S.C. Chen, et al., Hazardous characteristics of charge and discharge of lithium-ion batteries under adiabatic environment and hot environment, Int. J. Heat Mass Transf. 141 (2019) 419–431.

[13] J. Wang, J.J. Yang, W. Bai, et al., Thermal runaway and jet flame features of LIBs undergone high-rate charge/discharge: an investigation, J. Energy Chem. 103 (2025) 826–837, https://doi.org/10.1016/j.jechem.2024.12.004.

[14] K. Wang, D. Ouyang, X. Qian, et al., Early warning method and fire extinguishing technology of lithium-ion battery thermal runaway: a review, Energies 16 (7) (2023) 2960, https://doi.org/10.3390/en16072960.

[15] W. Mei, Z. Cheng, L. Wang, et al., Thermal hazard comparison and assessment of Li-ion battery and Na-ion battery, J. Energy Chem. 102 (2025) 18–26, https://doi.org/10.1016/j.jechem.2024.10.036.

[16] X. Jiang, Y. Hou, Y. Wang, et al., Solvation chemistry enables eutectogels with ultrahigh autofluorescence, toughness, and adhesion under extreme environments, Adv. Funct. Mater. 35 (2) (2024) 2412313, https://doi.org/10.1002/adfm.202412313.

[17] W. Liu, Y. Zhou, J. Wang, et al., Enhancing low-temperature CO removal in complex flue gases: a study on La and Cu doped $Co_3O_4$ catalysts under real-world combustion environment, J. Hazard. Mater. 470 (2024) 134174, https://doi.org/10.1016/j.jhazmat.2024.134174.

[18] J. Wang, Y. Zhou, Z. Wang, et al., Fire-resistant and mechanically-robust phosphorus-doped $MoS_2$/epoxy composite as barrier of the thermal runaway propagation of lithium-ion batteries, Chem. Eng. J. 497 (2024) 154866, https://doi.org/10.1016/j.cej.2024.154866.

[19] W.D. He, Y.Y. Li, L. Ni, et al., Effect of stabilizer EDTA on the thermal hazard of green synthesis process of adipic acid and development of microchannel continuous flow process, Emerg. Manag. Sci. Technol. 3 (2023) 22. 〈https://doi.org/10.48130/EMST-2023-0022〉.

[20] J. Hu, T. Liu, X.S. Wang, Z.G. Wang, L.S. Wu, Investigation on thermal runaway of 18,650 lithium-ion battery under thermal abuse coupled with charging, J. Energy Storage 51 (2022) 104482, https://doi.org/10.1016/j.est.2022.104482.

[21] K. Wang, D. Wu, C. Chang, et al., Charging rate effect on overcharge-induced thermal runaway characteristics and gas venting behaviors for commercial lithium

iron phosphate batteries, J. Clean. Prod. 434 (2024) 139992, https://doi.org/10.1016/j.jclepro.2023.139992.

[22] X.M. Xu, X.D. Sun, L.J. Zhao, et al., Research on thermal runaway characteristics of NCM lithium-ion battery under thermal-electrical coupling abuse, Ionics 28 (12) (2022) 5449–5467, https://doi.org/10.1007/S11581-022-04730-0.

[23] J.L. Liu, Z.H. Huang, J.H. Sun, et al., Heat generation and thermal runaway of lithium-ion battery induced by slight overcharging cycling, J. Power Sources 526 (2022) 231136, https://doi.org/10.1016/j.jpowsour.2022.231136.

[24] D.P. Kong, H.L. Zhao, P. Ping, et al., Effect of low temperature on thermal runaway and fire behaviors of 18650 lithium-ion battery: a comprehensive experimental study, Process Saf. Environ. Prot. 174 (2023) 448–459, https://doi.org/10.1016/j.psep.2023.04.017.

[25] S. Ohneseit, P. Finster, C. Floras, et al., Thermal and mechanical safety assessment of type 21700 lithium-ion batteries with NMC, NCA and LFP cathodes–investigation of cell abuse by means of accelerating rate calorimetry (ARC), Batteries 9 (5) (2023) 237, https://doi.org/10.3390/batteries9050237.

[26] Z.H. Huang, X. Li, Q.S. Wang, et al., Experimental investigation on thermal runaway propagation of large format lithium-ion battery modules with two cathodes, Int. J. Heat Mass Transf. 172 (2021) 121077, https://doi.org/10.1016/j.ijheatmasstransfer.2021.121077.

[27] B.B. Mao, P.F. Huang, H.D. Chen, et al., Self-heating reaction and thermal runaway criticality of the lithium-ion battery, Int. J. Heat Mass Transf. 149 (2020) 119178, https://doi.org/10.1016/j.ijheatmasstransfer.2019.119178.

[28] P.J. Liu, H.L. Sun, Y.T. Qiao, et al., Experimental study on the thermal runaway and fire behavior of $LiNi_{0.8}Co_{0.1}Mn_{0.1}O_2$ battery in open and confined spaces, Process Saf. Environ. Prot. 158 (2022) 711–726, https://doi.org/10.1016/j.psep.2021.12.056.

[29] Z.J. An, T.L. Shi, X.Z. Du, et al., Experimental study on the internal short circuit and failure mechanism of lithium-ion batteries under mechanical abuse conditions, J. Energy Storage 89 (2024) 111819, https://doi.org/10.1016/j.est.2024.111819.

[30] J.J. W, J.R. Jia, Z.H. Zhang, Research on the early warning mechanism for thermal runaway of lithium-ion power batteries in electric vehicles, Secur. Commun. Netw. 2022 (2022) 8573396, https://doi.org/10.1155/2022/8573396.

[31] X.Y. Dai, D.P. Kong, J. Du, et al., Investigation on effect of phase change material on the thermal runaway of lithium-ion battery and exploration of flame retardancy improvement, Process Saf. Environ. Prot. 159 (2021) 232–242, https://doi.org/10.1016/j.psep.2021.12.051.

[32] J. Mei, G.Q. Shi, Q. Li, et al., Experimental study on the effect of phase change material on thermal runaway characteristics of lithium-ion battery under different triggering methods, J. Energy Storage 75 (2024) 109832, https://doi.org/10.1016/j.est.2023.109832.

[33] Y.M. Li, Y.X. Lu, C.L. Zhao, et al., Recent advances of electrode materials for low-cost sodium-ion batteries towards practical application for grid energy storage, Energy Storage Mater. 7 (2017) 130–151, https://doi.org/10.1016/j.ensm.2017.01.002.

[34] X.N. Feng, M.G. Ouyang, X. Liu, et al., Thermal runaway mechanism of lithium-ion battery for electric vehicles: a review, Energy Storage Mater. 10 (2018) 246–267, https://doi.org/10.1016/j.ensm.2017.05.013.

[35] M.Y. He, S.M. Liu, J.T. Wu, et al., Review of cathode materials for sodium-ion batteries, Prog. Solid State Chem. 74 (2024) 100452, https://doi.org/10.1016/j.progsolidstchem.2024.100452.

[36] H. Rabab, N. Damay, C. Forgez, et al., Equivalent circuit model for sodium-ion batteries with physical-based representations of their non-linearities, in: 2023 IEEE Vehicle Power and Propulsion Conference, VPPC. ⟨https://doi.org/10.1109/VPPC60535.2023.10403267⟩.

[37] D. Velumani, A. Bansal, Thermal behavior of lithium- and sodium-ion batteries: a review on heat generation, battery degradation, thermal runway-perspective and future directions, Energy Fuels 36 (23) (2022) 14000–14029, https://doi.org/10.1021/acs.energyfuels.2c02889.

[38] Y.B. Yue, Z.Z. Jia, Y.Q. Li, et al., Thermal runaway hazards comparison between sodium-ion and lithium-ion batteries using accelerating rate calorimetry, Process Saf. Environ. Prot. 189 (2024) 61–70, https://doi.org/10.1016/j.psep.2024.06.032.

[39] Y.Y. Xie, G.L. Xu, H.Y. Chen, et al., Probing thermal and chemical stability of $Na_xNi_{1/3}Fe_{1/3}Mn_{1/3}O_2$ cathode material toward safe sodium-ion batteries, Chem. Mater. 30 (15) (2018) 4909–4918, https://doi.org/10.1021/acs.chemmater.8b00047.

[40] Q. Zhou, Y.Q. Li, et al., Thermal stability of high power 26650-type cylindrical Na-ion batteries, Chin. Phys. Lett. 38 (7) (2021) 076501, https://doi.org/10.1088/0256-307X/38/7/076501.

[41] A. Bordes, G. Marlair, A. Zantman, et al., Safety evaluation of a sodium-ion cell: assessment of vent gas emissions under thermal runaway, ACS Energy Lett. 7 (10) (2022) 3386–3391, https://doi.org/10.1021/acsenergylett.2c01667.

[42] B. Li, Y. Liu, X.H. Han, et al., Electrospun nanofiber surface-modified polyethylene separator for enhanced cycling stability and low-temperature performance of sodium-ion batteries, Chem. Eng. J. 501 (2024) 157803, https://doi.org/10.1016/j.cej.2024.157803.

[43] Z. Li, B.Q. Li, C.X. Bi, et al., A review of lithium–sulfur batteries at different working conditions: the role of ambient temperature, external force, and electromagnetic field, Mater. Sci. Eng.: R: Rep. 164 (2025) 100955, https://doi.org/10.1016/j.mser.2025.100955.

[44] M.Y. Liu, S.T. Zhong, X.Y. Zhu, et al., Failure mechanism and behaviors of lithium-ion battery under high discharging rate condition, J. Energy Storage 101 (2024) 113811, https://doi.org/10.1016/j.est.2024.113811.

[45] R.X. Wang, X. Zhou, Y. Wang, et al., Degradation analysis of lithium-ion batteries under ultrahigh-rate discharge profile, Appl. Energy 376 (2024) 124241, https://doi.org/10.1016/j.apenergy.2024.124241.

[46] C.B. Jin, T.F. Liu, O.W. Sheng, et al., Rejuvenating dead lithium supply in lithium metal anodes by iodine redox, Nat. Energy 6 (4) (2021) 378–387, https://doi.org/10.1038/S41560-021-00789-7.

[47] X.K. Lin, K. Khosravinia, X.S. Hu, et al., Lithium plating mechanism, detection, and mitigation in lithium-ion batteries, Prog. Energy Combust. Sci. 87 (2021) 10095, https://doi.org/10.1016/j.pecs.2021.100953.

[48] F.L. Chu, J.L. Hu, J. Tian, et al., In situ plating of porous mg network layer to reinforce anode dendrite suppression in Li-metal batteries, ACS Appl. Mater. Interfaces 10 (15) (2018) 12678–12689, https://doi.org/10.1021/acsami.8b00989.